Heterojunction α-Fe₂O₃/ZnO films with enhanced photocatalytic properties grown by aerosol-assisted chemical vapour deposition

Arreerat Jiamprasertboon,[a,b] Andreas Kafizas,[c,d] Michael Sachs,[d] Min Ling,[b] Abdullah M. Alotaibi,[b] Yao Lu,[e] Theeranun Siritanon,[a] Ivan P. Parkin,[b] and Claire J. Carmalt*[b]

[a] School of Chemistry, Institute of Science, Suranaree University of Technology, 111 University Avenue, Muang, Nakhon Ratchasima, 30000, Thailand

[b] Material Chemistry Centre, Department of Chemistry, University College London, 20 Gordon Street, London, WC1H 0AJ, UK

[c] Department of Chemistry, Imperial College London, South Kensington, London, SW7 2AZ, United Kingdom

[d] The Grantham Institute, Imperial College London, South Kensington, London, SW7 2AZ, United Kingdom

[e] Department of Mechanical Engineering, University College London, London, WC1E 7JE, United Kingdom

*Corresponding author, E-mail: c.j.carmalt@ucl.ac.uk

Graphical abstract
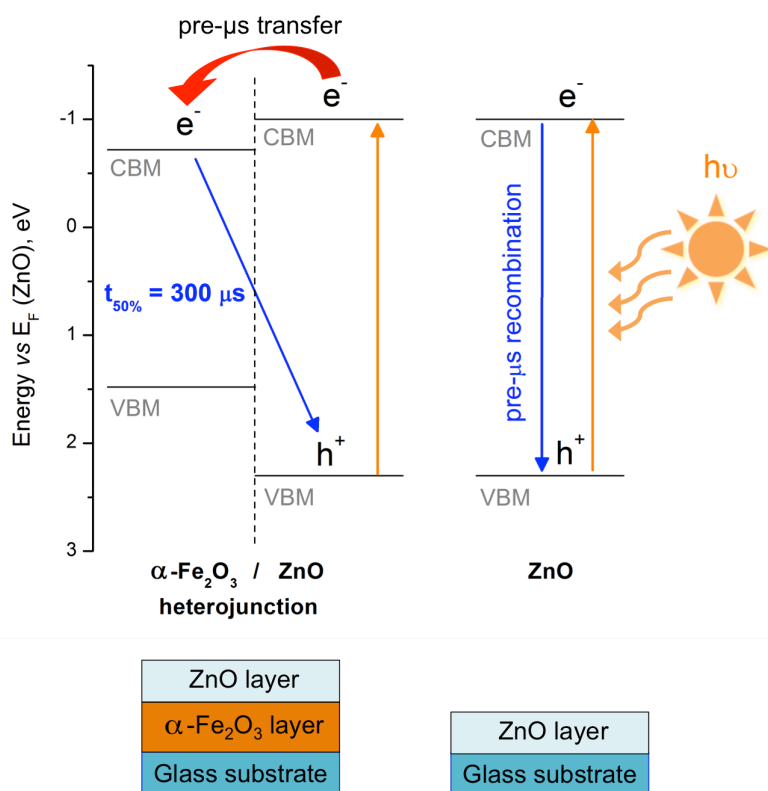
Heterojunction α-Fe$_2$O$_3$/ZnO film, grown using a simple aerosol-assisted CVD technique, showed enhanced photocatalytic activity. This was attributed to improved charge carrier separation, with electron transfer across the type-I heterojunction interface from ZnO into α-Fe$_2$O$_3$.

Highlights

- Robust, heterojunction coatings of α-Fe$_2$O$_3$/ZnO successfully prepared by AA-CVD.
- Coatings showed enhanced photocatalytic activity to the degradation of stearic acid.
- Charge carrier behavior in this system was studied by TAS for the first time.
- Mechanism of charge carrier separation determined by both TAS and XPS.

Abstract

Type-I heterojunction films of α-Fe$_2$O$_3$/ZnO are reported herein as a non-titania based photocatalyst that shows remarkable enhancement in the photocatalytic properties towards stearic acid degradation under UVA light exposure (λ = 365 nm), with a quantum efficiency of ξ = 4.42 $\pm$ 1.54 $\times$ 10^{-4} molecules degraded/photon, which was about 16 times greater than

that of α-Fe$_2$O$_3$, and 2.5 times greater than that of ZnO. As the degradation of stearic acid requires 104 electron transfers for each molecule, this represents an overall quantum efficiency of 4.60% for the α-Fe$_2$O$_3$/ZnO heterojunction. Time-resolved transient absorption spectroscopy (TAS) revealed the charge carrier behavior responsible for this increase in activity. Photogenerated electrons, formed in the ZnO layer, were transferred into the α-Fe$_2$O$_3$ layer on the pre-μs timescale, which reduced electron-hole recombination. This increased the lifetime of photogenerated holes formed in ZnO that oxidise stearic acid. The heterojunction α-Fe$_2$O$_3$/ZnO films grown herein show potential environmental applications as coatings for self-cleaning windows and surfaces.

Keywords

Hematite; Films; Heterojunctions; Photocatalysis; Aerosol-Assisted CVD

Introduction

The need for sustainable development has never been more vital. Climate change, caused primarily by the excessive use of fossil fuels and CO$_2$ release, often goes hand-in-hand with environmental issues, such as air pollution. Photocatalytic coatings are being developed, that use sunlight to break down pollutants, have been applied in a wide range of commercial products; including windows (*e.g.* Pilkington NSG, Activ^{TM}), tiles (*e.g.* TOTO, Hydrotect^{TM}), paints (*e.g.* Boysen, KNOxOUT^{TM}) and air purifiers (*e.g.* Hextio). The market for photocatalytic products is forecast to grow at a compound annual growth rate of 12.6% with a market value of ~\$2.9 billion by 2020.[1]

TiO$_2$ is the most widely studied photocatalyst, and the only photocatalyst to be applied commercially because of its high performance, low cost, durability and chemical stability.[2] However, the relatively wide bandgap energy of TiO$_2$ (*e.g.* anatase, ~3.2 eV) falls in the UV region of the electromagnetic spectrum, and can thus harness only ~4% of the solar spectrum. This severely limits the efficiency of TiO$_2$ for outdoor applications, and moreover, makes it unsuitable for indoor use with standard indoor lighting. Therefore, in order to improve the outdoor efficacy and indoor use of photocatalysts, researchers have attempted to develop materials with bandgap energies that fall in the visible.[3]

Various strategies have been applied in the development of visible light active photocatalysts, including impurity doping (*e.g.* N:TiO$_2$),[4] surface modification (*e.g.* phosphates),[5] nanostructuring (*e.g.* nanoneedles)[6] and the use of co-catalysts (*e.g.* Pt).[7]

However, recent studies have shown that one of the most promising strategies for improving photocatalytic activity is to form a heterojunction.[8] A heterojunction is defined as the interface between two dissimilar semiconductors. Recent studies have shown that heterojunctions can better spatially separate photogenerated charge and sufficiently prolong their lifetime to carry out kinetically sluggish photocatalytic reactions.[9] Various heterojunctions have shown promising synergetic enhancements in photocatalytic activity, including: Cu_2O/TiO_2, WO_3/TiO_2 and $WO_3/BiVO_4$.[9a, 10]. In fact, the benchmark photocatalyst, P25 Evonik (formerly Degussa), is a heterojunction composed of the anatase and rutile phases of TiO_2.[11]

Hematite (α-Fe_2O_3) has a narrow bandgap of 2.3 eV,[12] capable of absorbing ~20% of the solar spectrum, [13] and has shown promising activity as a visible-light active photocatalyst.[14] The earth's crust contains 6.3 wt.% iron, and is the fourth most common element. Moreover, α-Fe_2O_3 is a highly stable form of iron (otherwise known as rust). Hematite has been combined with a range of materials to form heterojunctions (*e.g.* WO_3/α-Fe_2O_3,[15] α-Fe_2O_3/SnO_2,[16] Si/α-Fe_2O_3,[17] α-Fe_2O_3/C coated g-C_3N_4)[18] many of which have shown enhanced activity for applications in solar energy conversion. Zinc oxide (ZnO) is also a promising photocatalyst, with high thermal and chemical stability, ubiquity and low cost.[19] Some previous studies have investigated α-Fe_2O_3/ZnO heterojunctions, which showed promising photocatalytic activity for pollutant degradation, *e.g.* dichloroacetic acid (DCA),[20] rhodamine Blue (RhB)[21] and pentachlorophenol (PCP),[22] under either UV or visible light irradiation. However, clear evidence on how this heterojunction system separates charge, and thereby improves photocatalytic activity, is yet to be demonstrated.

Herein, we grow film coatings of the α-Fe_2O_3/ZnO heterojunction using aerosol-assisted chemical vapour deposition (AACVD); a facile, inexpensive and scalable thin film deposition technique,[23] which has previously been used to prepare a variety of high quality films with controllable morphology, thickness and crystal structure.[24] In this study, we grow both α-Fe_2O_3/ZnO and ZnO/α-Fe_2O_3 heterojunctions, where the ZnO and α-Fe_2O_3 layers, respectively, are present at the surface of the coatings. We measure the photocatalytic activity of these heterojunction coatings against stearic acid under UVA light irradiation, and find significantly enhanced activity in the α-Fe_2O_3/ZnO heterojunction, with respect to the parent materials ZnO and α-Fe_2O_3. However, the ZnO/α-Fe_2O_3 heterojunction showed no marked improvement. Using transient absorption spectroscopy (TAS), we monitor the time-resolved charge carrier behavior in this heterojunction system, for the first time, and determine the

mechanism by which this type I straddling gap heterojunction separates charge, and thereby enhances photocatalytic activity in α-Fe$_2$O$_3$/ZnO.

Results and discussion

ZnO films were deposited from Zn(OAc)$_2$.2H$_2$O, and α-Fe$_2$O$_3$ films were grown from Fe(acac)$_3$, both carried in methanol *via* AACVD at 500 °C under a flow of N$_2$. As deposited films of ZnO were highly transparent, and likely contained little carbon contamination, whereas, as deposited films of α-Fe$_2$O$_3$ were brown/black in colour, and likely contained a some level of carbon contamination. We attribute this to the incomplete decomposition of the acac ligands, of the Fe(acac)$_3$ precursor, under the AACVD conditions used herein. However, post annealing in air resulted in the removal of carbon, and the formation of crystalline, orange-coloured, α-Fe$_2$O$_3$ films. In this study, both α-Fe$_2$O$_3$/ZnO and ZnO/α-Fe$_2$O$_3$ heterojunctions, where the ZnO and α-Fe$_2$O$_3$ layers are present at the surface of the coatings respectively, were grown using AACVD, from distinct depositions of each layer, using Fe(acac)$_3$ or Zn(OAc)$_2$·2H$_2$O in methanol at 500 °C. The α-Fe$_2$O$_3$/ZnO and ZnO/α-Fe$_2$O$_3$ heterojunctions were both orange in appearance. All films were stable to dissolution in common solvents such as methanol, acetone, isopropanol and chloroform.

The crystal structure adopted by the coatings was determined by XRD, as shown in Figure 1a. The single layer coatings were indexed as phase-pure α-Fe$_2$O$_3$ (hematite, R-3c) and ZnO (zincite, *P6$_3$mc*).[25] Showing no change, the bi-layer heterojunction coatings were composed of both hematite and zincite. Both hematite and zincite are the most thermodynamically stable forms of Fe$_2$O$_3$ and ZnO at ambient conditions, respectively. No other phases were detected. Cell parameters *a, c* and cell volume V were obtained using Le Bail refinement and the average crystallite sizes were calculated using the Scherrer equation (Table 1). Similar cell parameters were observed in both single layer and bi-layer heterojunction films, which indicated ion diffusion between layers was unsubstantial. The average crystallite size in both single layer films and α-Fe$_2$O$_3$/ZnO heterojunction films were similar.

Table 1. Lattice parameters *a*, *c* and Cell volume V obtained *via* Le Bail refinement and crystallite size obtained using the Scherrer's equation.

Films	Cell parameters (Å)		Cell volume (Å³)	Average crystallite size (Å)
	a	*c*	V	
Single layer				
α-Fe_2O_3	5.0358(37)	13.7775(154)	302.58(32)	299.7 ± 0.9
ZnO	3.2505(14)	5.2047(39)	47.62(6)	246.6 ± 0.6
α-Fe_2O_3/ZnO				
α-Fe_2O_3	5.0359(31)	13.7682(137)	302.39(27)	309.6 ± 0.8
ZnO	3.2509(11)	5.2064(28)	47.65(5)	246.4 ± 1.0
ZnO/α-Fe_2O_3				
α-Fe_2O_3	5.0364(9)	13.7648(43)	302.37(9)	234.9 ± 0.7
ZnO	3.2505(14)	5.2006(102)	47.65(9)	244.5 ± 0.3

The Raman spectra of α-Fe_2O_3, ZnO and α-Fe_2O_3/ZnO heterojunction films are illustrated in Figure 1b. The Raman scattering bands observed in the spectrum of the single layer α-Fe_2O_3 film corresponds to the hematite phase: A_{1g} (224 cm^{-1}, 494 cm^{-1}), E_g (243 cm^{-1}, 290 cm^{-1}, 409 cm^{-1}, 610 cm^{-1}).[26] However, no obvious bands were observed in the Raman spectra of ZnO and α-Fe_2O_3/ZnO heterojunction films.

The elemental composition and oxidation state at the surface of the coatings was determined using XPS. High-resolution XPS spectra of Fe 2p, Zn 2p and O 1s for the α-Fe_2O_3/ZnO heterojunction film are shown in Figure 1c. The XPS spectra of the single layer films are provided in the supporting information section (Figure S1, Table S1). Peaks observed at the binding energies of 710.1 eV and 723.3 eV represent Fe $2p_{3/2}$ and Fe $2p_{1/2}$ environments, respectively, and correspond to the presence of Fe^{3+}.[27] Zn $2p_{3/2}$ and Zn $2p_{1/2}$ environments were observed at binding energies of 1020.8 eV and 1043.9 eV respectively, and correspond to the presence of Zn^{2+}.[28] The O 1s environment can be separated into two peaks. The peak at 530.3 eV is attributed to O bonded to metal cations in the lattice, and the peak at 531.9 eV is attributed to O bonded to adventitious carbon (*e.g.* C-O, C=O bonds) and the chemisorption of O species such as O_2 and OH.[29] An XPS depth profile was carried out to determine the elemental composition with depth. In the α-Fe_2O_3/ZnO heterojunction film, only the Zn 2p and O 1s environments were observed with depth profiling from 500 to 2,500 s, indicating the presence of solely ZnO in the topmost layer (Table S1). The coexistence of Fe 2p, Zn 2p and O 1s environments was observed with depth profiling from 5,000 to 35,000 s (Table S1). It was found that Fe was mostly detected in deeper level of the multilayer film

where the α-Fe_2O_3 layer was grown before the ZnO layer. XPS depth profile analysis of α-Fe_2O_3 and ZnO films was also carried out (Figure S1). In α-Fe_2O_3 films, high levels of carbon were present both at the surface (~60%, no sputtering) and sub-surface (~70%, 2,500 s of Ar sputtering), which indicated the incomplete decomposition of the acac ligands in the decompostion of $Fe(acac)_3$ to form α-Fe_2O_3. However, in ZnO films, only adventitious carbon was observed at the surface (~80%, no sputtering), with almost no carbon being present in the sub-surface (~1.4%, after 2,500 s of Ar sputtering). This indicated that the reaction of $Zn(OAc)_2$ precursor was cleaner in forming ZnO films.

The chemical composition of the α-Fe_2O_3/ZnO heterojunction film was determined using EDS; Fe was not observed at a beam energy of 10 kV, but was detected at a beam energy of 15 - 20 kV as the electron beam probed deeper (see supporting information, Figure S2).
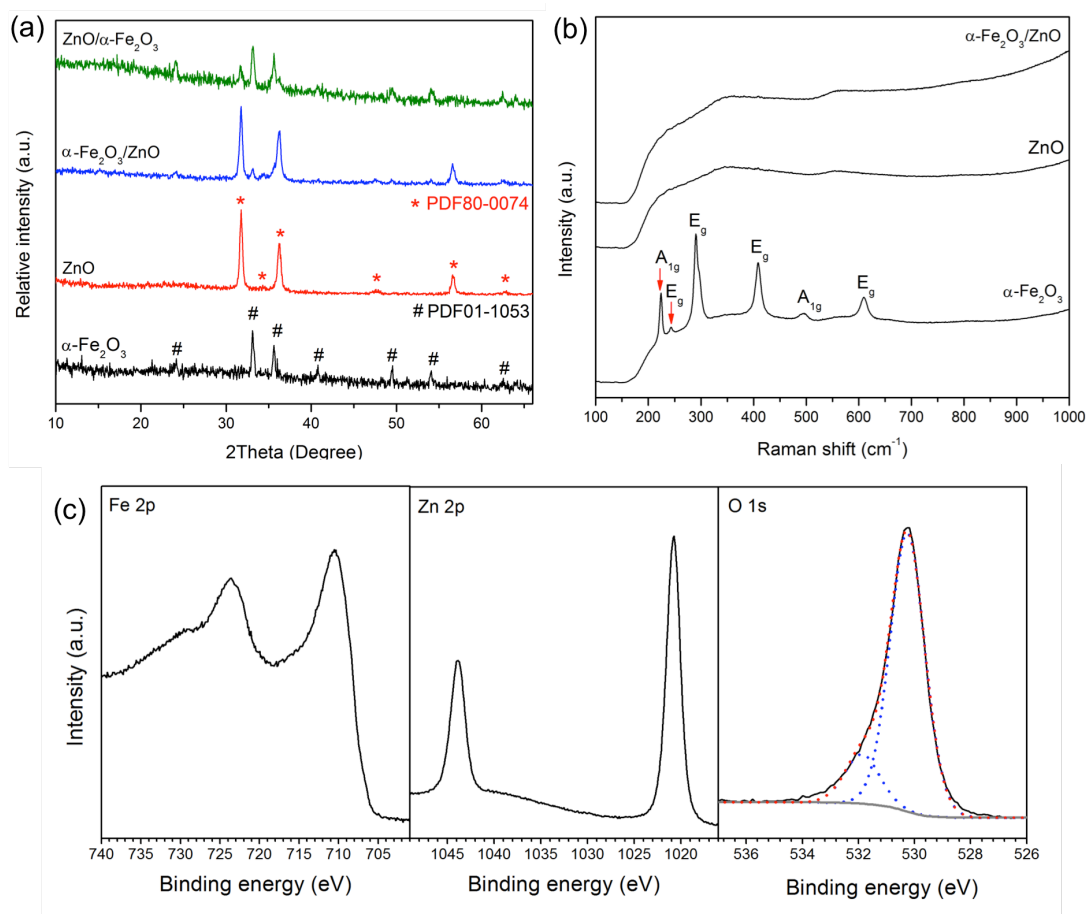
Figure 1. Physical characterization of the single layer films, α-Fe_2O_3 and ZnO, and the heterojunction films, α-Fe_2O_3/ZnO and ZnO/α-Fe_2O_3. a) XRD patterns. b) Raman spectra. c) XPS core level spectra of the α-Fe_2O_3/ZnO heterojunction; the Zn 2p region was measured at the surface, whereas the Fe 2p and O 1s regions were measured after sputtering for 25,000 s.

SEM images are shown in Figure 2. Films of α-Fe$_2$O$_3$ were primarily smooth and contained some pinholes; forming a densely packed structure composed of rounded particles of less than 100 nm in diameter. Films of ZnO were composed of well-distributed worm-like particles, roughly 50 × 100 nm in size. In case of heterojunction films, the α-Fe$_2$O$_3$/ZnO film exhibited an agglomeration of round-like particles of around 100 nm while the ZnO/α-Fe$_2$O$_3$ film showed a densely smooth morphology. It can be seen that surface morphology of all films before and after photocatalytic testing are similar, which implies good chemical and photochemical stability. Film thickness was estimated from side-on SEM images: ~1,000 nm for α-Fe$_2$O$_3$ film, ~700 nm for ZnO film, ~990 nm/~680 nm for the α-Fe$_2$O$_3$/ZnO heterojunction films and ~750 nm/~660 nm for the ZnO/α-Fe$_2$O$_3$ heterojunction films.
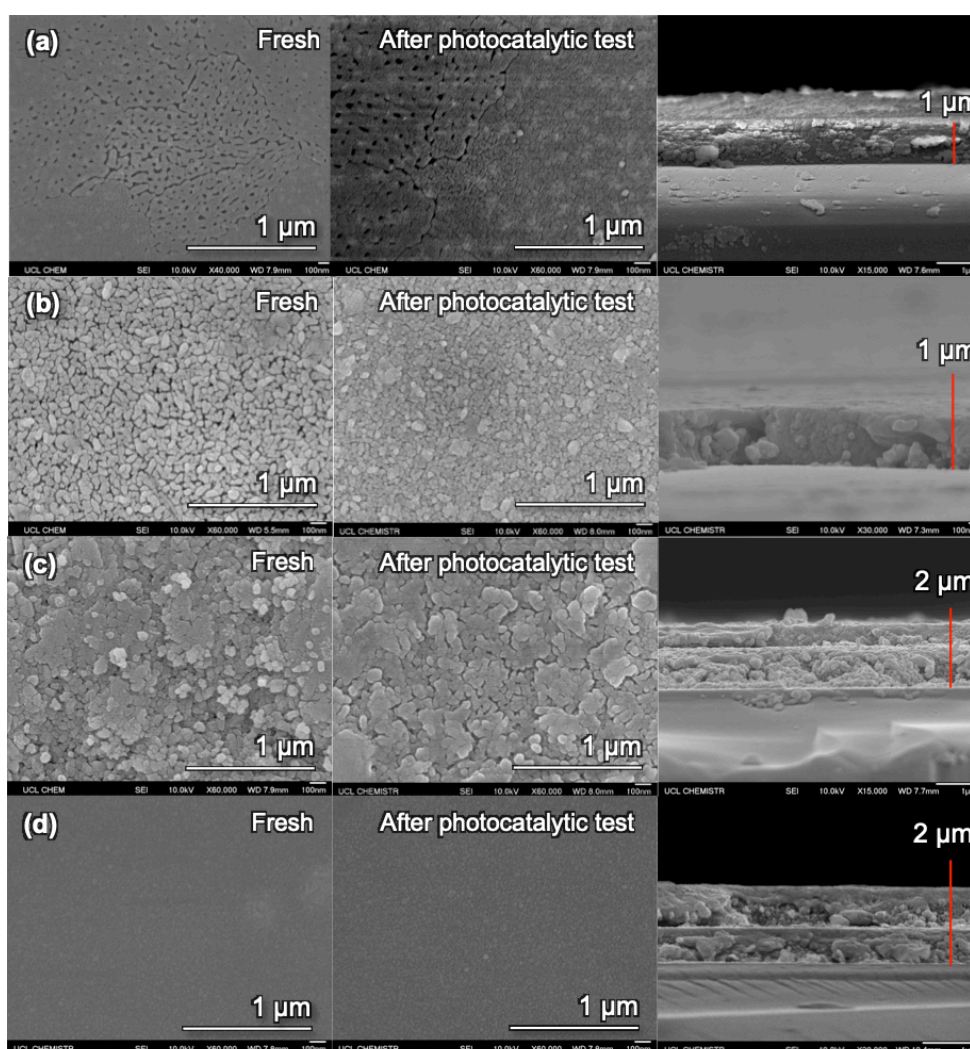

Figure 2. SEM images of a) α-Fe$_2$O$_3$, b) ZnO and heterojunction films of c) α-Fe$_2$O$_3$/ZnO and d) ZnO/α-Fe$_2$O$_3$, showing the film surface morphology of a fresh film (left), after photocatalytic testing (middle) and cross-sectional images (right).

The photocatalytic properties of films were investigated towards the degradation of stearic acid under UVA light irradiation. Stearic acid is stable under UV light exposure; therefore, it is widely used as a model pollutant for the study of photocatalytic activity.[30] The chemical reaction can be described by:

$$CH_3(CH_2)_{16}CO_2H + 26O_2 \xrightarrow{h\nu \geq Eg} 18CO_2 + 18H_2O \tag{1}$$
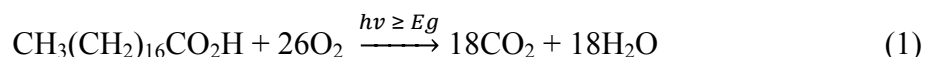
Previous work by Mills and Wang, showed that the photocatalytic oxidation of stearic acid results in its mineralization to CO_2, with little by-product formation (> 90% yield).[30] The efficiency is typically reported as the formal quantum efficiency (ξ), which determines the steric acid molecules degraded per incident photon. Figure 3 shows a plot of the quantum efficiencies, ξ, obtained for the films examined herein. In this study, uncoated glass was used as a blank, and Pilkington Activ[TM] self-cleaning glass was used as a reference commercial standard. For the single layer films, ZnO ($\xi = 1.76 \pm 0.13 \times 10^{-4}$ molecules/photon) was substantially more photocatalytically active than α-Fe$_2$O$_3$ ($\xi = 0.13 \pm 0.09 \times 10^{-4}$ molecules/photon). Importantly, the photocatalytic performance of the α-Fe$_2$O$_3$/ZnO heterojunction ($\xi = 4.42 \pm 1.54 \times 10^{-4}$ molecules/photon) was substantially higher, with the efficiency increasing by a factor of 16 relative to α-Fe$_2$O$_3$ and ~2.5 relative to ZnO. This value is comparable to P25 Degussa reported by Mills and co-workers ($\xi = 4.68 \pm 1.54 \times 10^{-4}$ molecules/photon).[31] Interestingly, the reverse architecture, the ZnO/α-Fe$_2$O$_3$ heterojunction, showed low activity ($\xi = 0.48 \pm 0.38 \times 10^{-4}$ molecules/photon).
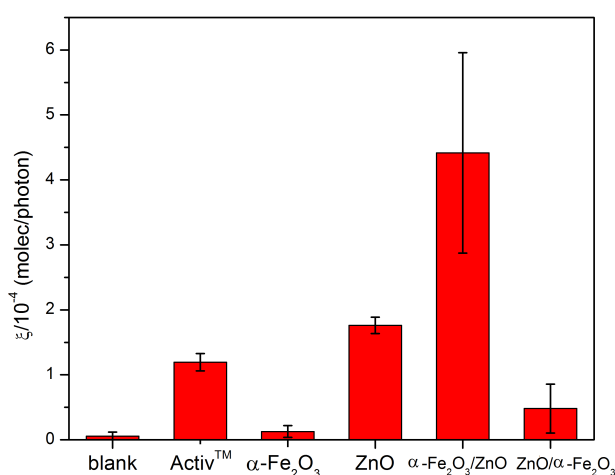
Figure 3. The formal quantum efficiency (ξ) for the photocatalytic degradation of stearic acid using UVA light (molecules degraded/ photon). Uncoated glass was used as the blank; Pilkington Activ[TM] self-cleaning glass was used as reference commerical standard.

A significant enhancement in photocatalytic activity was found in the heterojunction film where the ZnO layer was on the top. UV-visible transmittance spectra of the heterojunction film was similar to that of the α-Fe$_2$O$_3$ film (Figure 4), showing no substantial change in the optical properties of the coatings. The optical bandgaps, determined from Tauc plots (Figure S4), were similar to literature values (α-Fe$_2$O$_3$, E$_{bg}$ direct ~2.10 eV, E$_{bg}$ indirect ~2.15 eV;[32] ZnO E$_{bg}$ direct ~3.30 eV).[33]

Specific surface area is an important factor that can influence photocatalytic activity. AFM was used to quantify surface area (Figure S5). However, since the surface areas were similar for both single layer and heterojunction films (Table S2), the improved photocatalytic properties found in the α-Fe$_2$O$_3$/ZnO heterojunction could not be ascribed to any change in surface area.
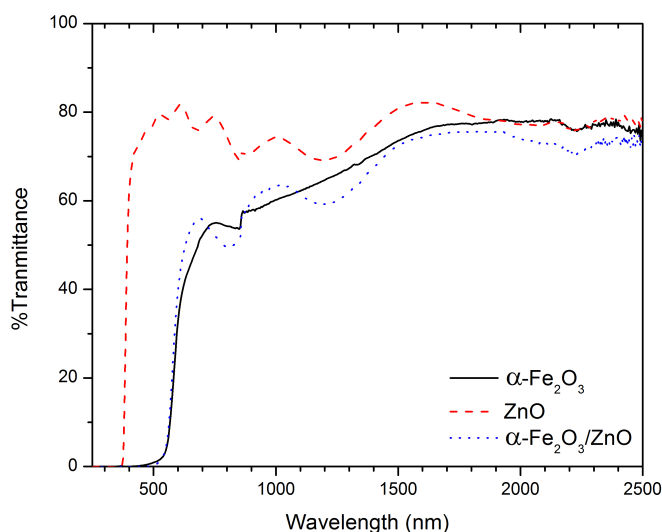
Figure 4. Transmittance spectra of α-Fe$_2$O$_3$, ZnO and α-Fe$_2$O$_3$/ZnO heterojunction films in the UV/Visible/NIR region.

Transient absorption spectroscopy (TAS) was used to study the charge carrier dynamics in the heterojunction films (α-Fe$_2$O$_3$/ZnO and ZnO/α-Fe$_2$O$_3$), and parent materials (α-Fe$_2$O$_3$ and ZnO) on the microsecond to second timescale. Either UV (355 nm) or visible light (500 nm) laser excitation was used. Electron and hole carriers in metal oxide semiconductor photocatalysts typically absorb in the UV-visible region (*e.g.* TiO$_2$, WO$_3$, α-Fe$_2$O$_3$, BiVO$_4$, *etc.*).[34] TAS has been used to monitor the charge carrier dynamics in a number of semiconductor photocatalysts; including the kinetics of photocatalytic processes and charge transfer behaviour in heterojunction systems such as WO$_3$/BiVO$_4$ and WO$_3$/TiO$_2$.[9]

In our TAS studies, the ZnO film showed no significant transient absorption signal over these timescales (Figure S6), which was attributed to dominant electron-hole recombination on the pre-μs timescale (*i.e.* before the time resolution of our measurements). However, under UV 355 nm excitation, the α-Fe$_2$O$_3$ film showed strong transient absorption signals, with charge carriers recombining with power law decay dynamics ($t_{50\%}$ ~300 μs from 10 μs; Figure S7). The transient absorption spectrum was broad across the visible region, similar to previous studies.[35] Under 500 nm excitation, similar charge carrier behaviour was observed (Figure S8), with the kinetics and spectral shape differing only marginally ($t_{50\%}$ ~100 μs from 10 μs).

However, when exciting with UV light at the ZnO side, charge carrier lifetime in the ZnO layer was significantly enhanced by the formation of an α-Fe$_2$O$_3$/ZnO heterojunction (Figure S9a). This heterojunction showed a peak positive absorption in the green that decreased into the red and became a bleach (*i.e.* a negative signal). At the probe wavelength of 600 nm, charge carrier recombination showed power law recombination dynamics ($t_{50\%}$ ~300 μs from 10 μs), similar to α-Fe$_2$O$_3$. This enhancement in charge carrier lifetime was only observed when the junction was irradiated at the ZnO side using UV light. When the α-Fe$_2$O$_3$/ZnO heterojunction was irradiated at the α-Fe$_2$O$_3$ side (Figure S9b), using either UV or visible light, charge carriers were primarily formed in the α-Fe$_2$O$_3$ layer. These charges were most likely static, and transferred into the ZnO layer, as the transient absorption spectrum and kinetics were analogous to single layer α-Fe$_2$O$_3$ films (Figures S7 and S8).

Chemical scavenger studies were carried out to identify the nature of the long-lived charges found in ZnO when present in the α-Fe$_2$O$_3$/ZnO heterojunction. ZnO nanopowder was used for chemical scavenger studies. Films were not used, as they did not show sufficient scavenging activity (*i.e.* the quantum yield of scavenging was too low, and electron-hole recombination signals dominated).

Chemical scavenging was studied in three chemically different environments: (i) acetonitrile [inert], (ii) methanol [hole scavenger] and (iii) aqueous silver nitrate [electron scavenger].[34b, 36] In acetonitrile, no signals were observed; similar to ZnO films when not present in a junction (Figure 5a). In methanol and silver nitrate, long-lived signals were observed, and were attributed to the presence of long-lived electrons and holes respectively that formed distinct spectra; with electrons absorbing most strongly in the near infrared and holes absorbing most strongly in the blue-green region of the visible (Figure 5a). Similar chemical scavenger behaviour was previously observed in TiO$_2$[36] and WO$_3$;[37] with holes

also absorbing most strongly in the blue and electrons in the red. This showed that the spectral signals observed in our α-Fe$_2$O$_3$/ZnO heterojunction, when exciting with UV laser light at the ZnO side, were most likely long-lived holes present in ZnO (Figure 5b). The increased longevity of this charge was attributed to the separation of photo-generated electrons, formed in ZnO, by transfer on the pre-μs timescale into α-Fe$_2$O$_3$; thereby inhibiting electron-hole recombination in ZnO (Figure S6). This observation was in line with our band alignment diagram, determined using XPS spectroscopy (Figures S9 and S10, see supporting information for more details), which showed the formation of a type I straddling gap heterojunction with a thermodynamic driving force for the transfer of photo-generated electrons from ZnO into α-Fe$_2$O$_3$ (Figure 6). It should be noted that the charge carriers generated in α-Fe$_2$O$_3$ could not be transferred to ZnO under visible light irradiaiton; therefore, the photocatalytic properties were only enhanced under UV light (as shown by our photocatalytic activity studies in Figure 3).
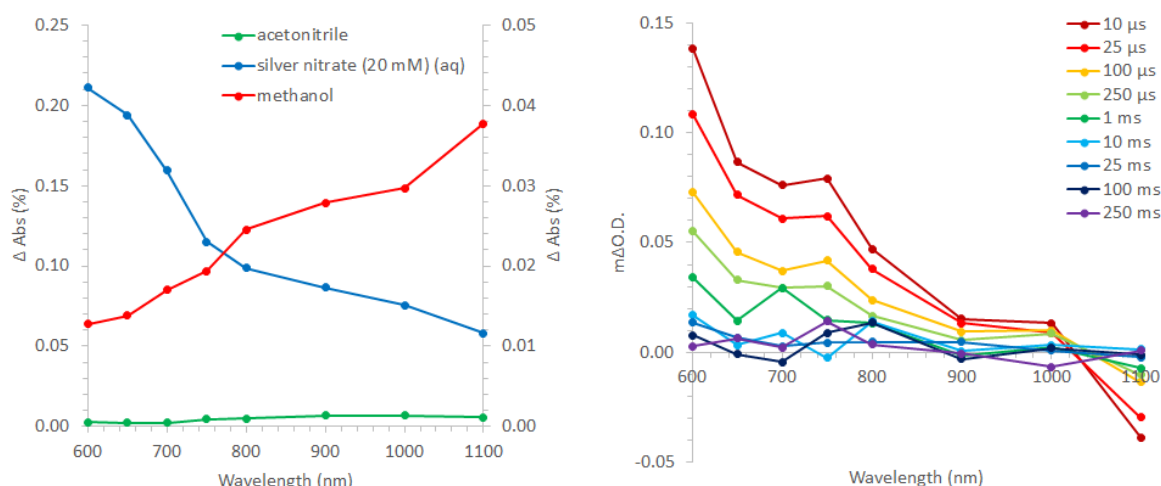
Figure 5. (a) Transient absorption spectra of ZnO nanopowder, 100 ms after a laser pulse (λ_{exc} = 355 nm, ~0.5 mJ.cm^{-2}, 6 ns pulse width) when dispersed in acetonitrile, aqueous silver nitrate or methanol. (b) Transient absorption spectra of the α-Fe$_2$O$_3$/ZnO heterojunction at select times (λ_{exc} = 355 nm, ~0.5 mJ.cm^{-2}, 6 ns pulse width, 0.65 Hz), where the laser pump was directed at the ZnO layer first (*i.e.* front excitation).

Although there is a thermodynamic driving force for hole transfer from ZnO into α-Fe$_2$O$_3$, the short diffusion length of holes in ZnO inhibits this transfer (L_D < 250 nm).[38] As such, photo-generated holes, primarily formed at the surface of ZnO, are longer-lived due to

the enhanced spatial separation of photo-generated electrons into α-Fe$_2$O$_3$. Thus, these long-lived holes can more likely drive kinetically slow photocatalytic reactions at the surface, *e.g.*, hole reactions with water to form hydroxyl radicals, which typically take place on the millisecond timescale. Overall, our transient absorption studies corroborate our photocatalysis experiments, which show significant enhancements in activity in the α-Fe$_2$O$_3$/ZnO heterojunction with respect to the parent materials under UVA irradiation.
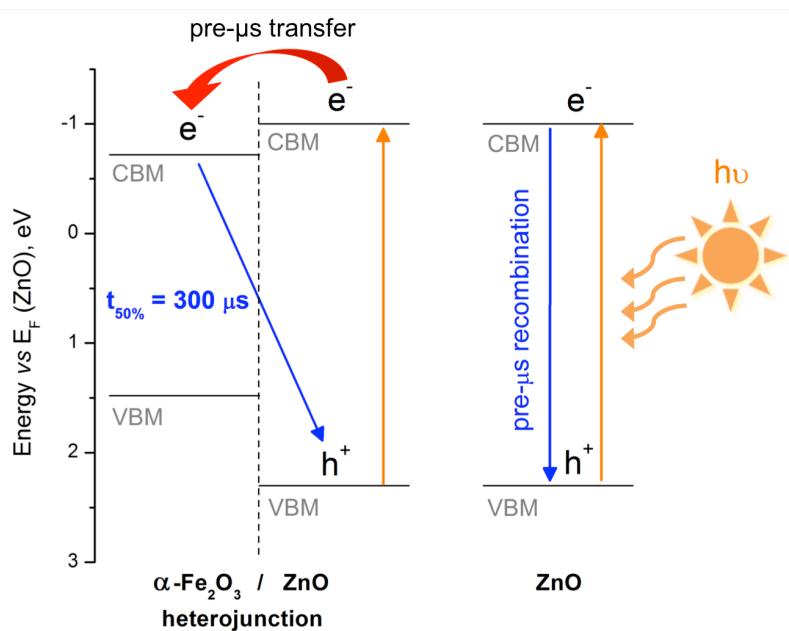
Figure 6. Band alignment diagram, determined using XPS, detailing charge transfer in the α-Fe$_2$O$_3$/ZnO heterojunction, determined from TAS measurements. The Fermi level energy of ZnO is set to 0 V on the energy scale (see supporting information for more details).

Conclusions

Films of α-Fe$_2$O$_3$, ZnO and their combinations to form the heterojunction bi-layers α-Fe$_2$O$_3$/ZnO and ZnO/α-Fe$_2$O$_3$ were grown using aerosol-assisted chemical vapour deposition (AACVD). The deposited films crystallised as hematite α-Fe$_2$O$_3$ and zincite ZnO; as identified by XRD. Both surface and depth-profile XPS spectra were used to identify elemental composition and oxidation state. This confirmed the presence of Fe^{3+} and Zn^{2+} at the surface of α-Fe$_2$O$_3$ and ZnO coatings respectively, as well as the formation of distinct α-Fe$_2$O$_3$ and ZnO layers in the heterojunction films. SEM images showed that the coatings were flat, dense structures that were stable to repeat photocatalytic testing.

The α-Fe$_2$O$_3$/ZnO heterojunction showed the highest photocatalytic activity to the degradation of stearic acid using UVA light ($\xi = 4.42 \pm 1.54 \times 10^{-4}$ molecules/photon), which was respectively ~16 and ~2.5 times greater than that of the α-Fe$_2$O$_3$ ($0.13 \pm 0.09 \times 10^{-4}$ molecules/photon) and ZnO ($1.76 \pm 0.13 \times 10^{-4}$ molecules/ photon) films. In contrast, the reverse architecture, the ZnO/α-Fe$_2$O$_3$ heterojunction, was far less active ($\xi = 0.48 \pm 0.38 \times 10^{-4}$ molecules/photon). As the degradation of stearic acid requires 104 electron transfers per molecule, this represents a quantum efficiency of 4.60% for the α-Fe$_2$O$_3$/ZnO heterojunction. TAS and XPS band alignment studies showed that the improved photocatalytic properties found in α-Fe$_2$O$_3$/ZnO was due to the formation of a type I straddling gap heterojunction, which promoted the separation of photo-generated electrons formed in ZnO into the α-Fe$_2$O$_3$ layer, thereby prolonging the lifetime of photo-generated holes formed in ZnO that drive photocatalytic oxidation processes.

Experimental Section
Film synthesis

All films were grown using aerosol assisted chemical vapor deposition (AACVD). Reagent grade chemicals of Zn(OAc)$_2$.2H$_2$O ($\geq$ 98%, Sigma-Aldrich) and Fe(acac)$_3$ (99.9%, Aldrich) were used as starting materials. Methanol (99.9%, Fisher Scientific) was used as the solvent. N$_2$ gas (99.99%, BOC) was used as a carrier gas.

The depositions of α-Fe$_2$O$_3$ and ZnO films were carried out using precursor solutions of Zn(OAc)$_2$.2H$_2$O (0.50 g, 2.28 mmol) in methanol (20 mL) and that of Fe(acac)$_3$ (0.50 g, 1.42 mmol) in methanol (60 mL), respectively. The solution was stirred until all precursors were dissolved (*ca*. 5-10 minutes). The glass substrate used was coated with the SiO$_2$ barrier layer of 50 mm to prevent diffusion of ions from the glass (*e.g.* Na, Ca, Mg *etc*) into the deposited film (Pilkington NSG Ltd). The SiO$_2$-coated glass substrate of dimensions 3.2 mm $\times$ 45 mm $\times$ 10 mm (thickness $\times$ length $\times$ breadth), was cleaned using detergent, isopropanol and acetone, respectively. The schematic illustration of the AACVD setup is displayed in Figure 7. The substrate was placed on the stainless steel plate of 4.8 cm $\times$ 15 cm and a carbon heating block was suspended over the substrate approximately 8 mm; the setup was enclosed in a quartz tube. In a typical deposition, the aerosol was produced from the humidification of the precursor solution, using a 'Liquifog' piezo ultrasonic humidifier (Johnson Matthey). The aerosol was then transferred to the AACVD reactor through the baffle by use of the N$_2$ carrier

gas. The films were deposited at 500 ºC, with α-Fe₂O₃ and ZnO grown using flow rates of 1.4 and 1.5 L/min, which were took ~35 and ~15 minutes, respectively. For α-Fe$_2$O$_3$/ZnO heterojunction films, the α-Fe$_2$O$_3$ layer was first grown on the SiO$_2$-coated glass substrate followed by the ZnO layer. For ZnO/α-Fe$_2$O$_3$ heterojunction films, the ZnO layer was first grown on the SiO$_2$-coated glass substrate followed by the α-Fe$_2$O$_3$ layer. The coatings were removed from the reactor after cooling under a continuous flow of N$_2$ gas to below 100 ºC. All films were subsequently annealed at 500 ºC for 3 hr in air.
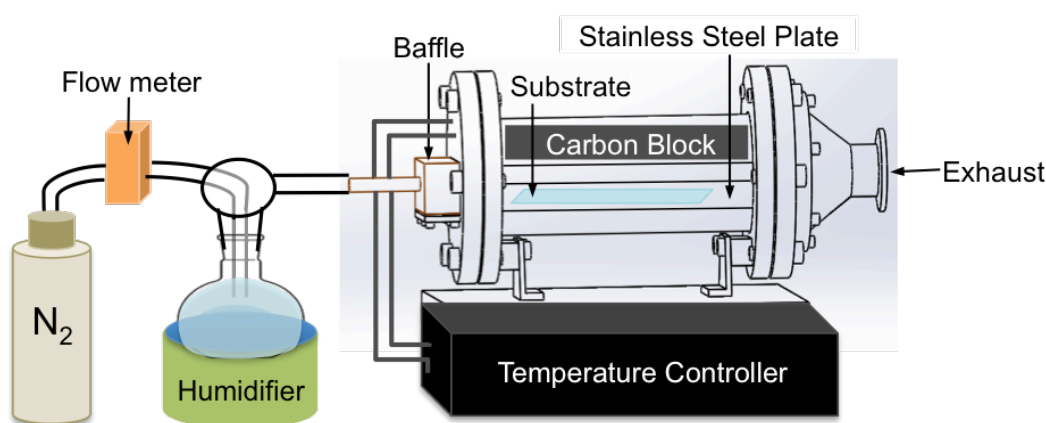
Figure 7. The schematic diagram of aerosol-assisted chemical vapour deposition (AACVD) setup.

Physical characterisation

A Bruker-Axs D8 X-ray diffractometer with parallel beam optics equipped with a PSD LynxEye silicon strip detector was carried out to confirm the phase purity of the films. X-rays were generated using monochromatic Cu K$_{\alpha1}$ and K$_{\alpha2}$ radiation (λ = 1.54056 Å and 1.54439 Å, respectively) with a voltage of 40 kV and a current of 40 mA. The grazing incident beam angle of 1° was used. X-ray diffraction (XRD) measurement was performed with 2θ range of 10-66° with a step size of 0.05° by a scan rate of 2 second per step. GSAS and EXPGUI software were utilised to obtain the cell parameters *via* Le Bail refinement.[39] Raman spectroscopy was conducted to obtain the structural fingerprint of chemical molecules in films. A Renishaw 1000 spectrometer equipped with a 633 nm red laser, calibrated using a silicon reference, was used to collect Raman spectra in the range of 100-1000 cm^{-1}. X-ray photoelectron spectroscopy (XPS) was used to check the elemental compositions and their oxidation states. The XPS spectra of Zn 2p, Fe 2p and O 1s were collected. Valence band (VB) was also performed with 200 scans. A Thermo Scientific K-alpha spectrometer with a monochromatic Al Kα radiation, a dual beam charge compensation system and constant pass

energy of 50 eV were utilised for the measurement. XPS depth profiling was carried out by bombarding the films with Ar^+ ion beam to etch the surface for 500 to 35,000 s. The obtained spectra were deconvoluted using CasaXPS software and the background was corrected using the Shirley method. The C 1s peak of 284.5 eV was used as a reference to calibrate binding energy.[40] A Perkin Elmer Lambda 950 UV/Vis/NIR Spectrophotometer was used to investigate the optical properties. Transmittance and reflectance spectra were collected with the range of 250-2500 nm. A JEOL JSM-6301F Field Emission instrument with an operated acceleration energy of 10 kV was used to get scanning electron microscope (SEM) images and side-on SEM images to probe the surface morphology and film thickness, respectively. Energy dispersive X-ray spectroscopy (EDS) was obtained using the Oxford instrumentals INCA Energy EDXA systems coupled with the SEM instrument. An atomic force microscope (AFM, Bruker Multi-mode 8) was used to study surface topology and roughness in term of root mean squared (R_q). The AFM images were obtained using the tip with the ScanAsyst tapping mode for probing the area of 1.0 μm × 1.0 μm for 512 scans.

Functional characterisation

The photocatalytic properties were determined using the test of stearic acid degradation under UVA light irradiation. The films were dipped in a 0.05 M stearic acid solution (chloroform was used as a solvent), producing a thin layer of steric acid coated on films. A Perkin Elmer RX-I instrument was utilised to collect Fourier transform infrared (FTIR) spectra in the range of 2700-3000 cm^{-1} to probe the C-H bond degradation. The measurement was performed in the absorbance mode under UVA (λ = 365 nm) light illumination of a 5 × 18 W blacklight-bulb (BLB) UVA lamps (Philips). The irradiation of 1 ± 0.1 mW cm^{-2} was used in the test, which was measured using a UVX meter (UVP). Formal quantum efficiency (ξ) value was acquired by the linear regression analysis of the initial 30-40% degradation steps, which are zero-order kinetics, with a conversion factor (1 cm^{-1} ≈ 9.7 × 10^{15} mol).[30]

Transient absorption spectroscopy (TAS), from the microsecond to second timescale, was measured in either transmission or diffuse reflection mode. A Nd:YAG laser (OPOTEK Opolette 355 II, ~6 ns pulse width) was used as the excitation source, generating 355 nm UV light from the third harmonic. This laser light could be converted into 500 nm visible light using an optical parametric oscillator. Either UV or visible laser light was transmitted to the

sample through a light guide. The power was adjusted so that the photon flux reaching the sample was analogous for UV and visible light experiments (~0.50 mJ.cm^{-2} for 355 nm light and ~0.38 mJ.cm^{-2} for 500 nm light). The laser was typically fired at a rate of 0.65 Hz (0.33 Hz for some scavenger experiments). The probe light was a 100 W Bentham IL1 quartz halogen lamp. Long pass filters (Comar Instruments) were placed between the lamp and sample to minimize short wavelength irradiation of the sample. Transient changes in absorption/diffuse reflectance from the sample was collected by a 2" diameter, 2" focal length lens and relayed to a monochromator (Oriel Cornerstone 130) and measured at select wavelengths between 600 and 1100 nm. Time-resolved intensity data was collected with a Si photodiode (Hamamatsu S3071). Data at times faster than 3.6 ms was recorded by an oscilloscope (Tektronics DPO3012) after passing through an amplifier box (Costronics), whereas data slower than 3.6 ms was simultaneously recorded on a National Instrument DAQ card (NI USB-6251). Each kinetic trace was obtained from the average of between 100 and 250 laser pulses. Acquisitions were triggered by a photodiode (Thorlabs DET10A) exposed to laser scatter. Data was acquired and processed using home-built software written in Labview. For film samples, transient changes in absorption were measured in transmission mode. Samples were measured in air. Our chemical scavenger experiments, conducted using ZnO nanopowder, were measured in diffuse reflectance mode since the nanopowders was highly scattering. As photo-induced changes in reflectance were low (< 1%), it was assumed that the transient signal was directly proportional to the concentration of excited species. Scavenger experiments were carried out in acetonitrile, methanol and aqueous silver nitrate (20 mM), where in each experiment 14 mg of ZnO nanopowders was dispersed in 1.0 ml of solution by sonication.

References

[1] M. Gagliardi, *BCC research*. 2015.

[2] K. M. Lee, C. W. Lai, K. S. Ngai, J. C. Juan, *Water Res.* **2016**, *88*, 428-448.

[3] F. E. Osterloh, *Chem. Soc. Rev.* **2013**, *42*, 2294.

[4] A. Kafizas, I. P. Parkin, *J. Mater. Chem.* **2010**, *20*, 2157.

[5] D. Zhao, C. Chen, Y. Wang, H. Ji, W. Ma, L. Zang, J. Zhao, *J. Phys. Chem. C* **2008**, *112*, 5993.

[6] A. Kafizas, L. Francàs, C. Sotelo-Vazquez, M. Ling, Y. Li, E. Glover, L. McCafferty, C. Blackman, J. Darr, I. Parkin, *J. Phys. Chem. C* **2017**, *121*, 5983.

[7] M. Tasbihi, K. Kočí, M. Edelmannová, I. Troppová, M. Reli, R. Schomäcker, *J. Photochem. Photobiol. A Chem.* **2018**, *366*, 72.

[8] a) J. Low, J. Yu, M. Jaroniec, S. Wageh, A. A. Al-Ghamdi, *Adv. Mater.* **2017**, *29*, 1601694; b) H. Wang, L. Zhang, Z. Chen, J. Hu, S. Li, Z. Wang, J. Liu, X. Wang, *Chem. Soc. Rev.* **2014**, *43*, 5234.

[9] a) C. Sotelo-Vazquez, R. Quesada-Cabrera, M. Ling, D. O. Scanlon, A. Kafizas, P. K. Thakur, T.-L. Lee, A. Taylor, G. W. Watson, R. G. Palgrave, J. R. Durrant, C. S. Blackman, I. P. Parkin, *Adv. Funct. Mater.* **2017**, *27*, 1605413; b) S. Selim, L. Francàs, M. García-Tecedor, S. Corby, C. Blackman, S. Gimenez, J. R. Durrant, A. Kafizas, *Chem. Sci.* **2019**, *10*, 2643.

[10] a) A. Paracchino, V. Laporte, K. Sivula, M. Grätzel, E. Thimsen, *Nat. Mater.* **2011**, *10*, 456; b) Y. Pihosh, I. Turkevych, K. Mawatari, J. Uemura, Y. Kazoe, S. Kosar, K. Makita, T. Sugaya, T. Matsui, D. Fujita, M. Tosa, M. Kondo, T. Kitamori, *Sci. Rep.* **2015**, *5*, 11141.

[11] a) D. O. Scanlon, C. W. Dunnill, J. Buckeridge, S. A. Shevlin, A. J. Logsdail, S. M. Woodley, C. R. A. Catlow, M. J. Powell, R. G. Palgrave, I. P. Parkin, G. W. Watson, T. W. Keal, P. Sherwood, A. Walsh, A. A. Sokol, *Nat. Mater.* **2013**, *12*, 798; b) A. Kafizas, X. Wang, S. R. Pendlebury, P. Barnes, M. Ling, C. Sotelo-Vazquez, R. Quesada-Cabrera, C. Li, I. P. Parkin, J. R. Durrant, *J. Phys. Chem. A* **2016**, *120*, 715.

[12] Y. Wang, Q. Wang, X. Zhan, F. Wang, M. Safdar, J. He, *Nanoscale* **2013**, *5*, 8326.

[13] K. Sivula, F. Le Formal, M. Grätzel, *ChemSusChem* **2011**, *4*, 432.

[14]　F. Le Formal, M. Grätzel, K. Sivula, *Adv. Funct. Mater.* **2010**, *20*, 1099.

[15]　K. Sivula, F. Le Formal, M. Grätzel, *Chem. Mater.* **2009**, *21*, 2862.

[16]　H. S. Han, S. Shin, J. H. Noh, I. S. Cho, K. S. Hong, *JOM* **2014**, *66*, 664.

[17]　L. Chen, S. Wu, D. Ma, A. Shang, X. Li, *Nano Energy* **2018**, *43*, 177.

[18]　L. Kong, J. Yan, P. Li, S. F. Liu, *ACS Sustain. Chem. Eng.* **2018**, *6*, 10436.

[19]　a) J. Hu, R. G. Gordon, *J. Appl. Phys.* **1992**, *71*, 880; b) M. R. Waugh, G. Hyett, I. P. Parkin, *Chem. Vap. Depos.* **2008**, *14*, 369.

[20]　S. Sakthivel, S. U. Geissen, D. W. Bahnemann, V. Murugesan, A. Vogelpohl, *J. Photochem. Photobiol. A Chem.* **2002**, *148*, 283.

[21]　a) W. Wu, S. Zhang, X. Xiao, J. Zhou, F. Ren, L. Sun, C. Jiang, *ACS Appl. Mater. Interfaces* **2012**, *4*, 3602; b) Y. Wu, L. Liu, X. Yu, J. Zhang, L. Li, C. Yan, B. Zhu, *Compos. Part B Eng.* **2018**, *137*, 178.

[22]　J. Xie, Z. Zhou, Y. Lian, Y. Hao, P. Li, Y. Wei, *Ceram. Int.* **2015**, *41*, 2622.

[23]　M. J. Powell, C. J. Carmalt, *Chem. - A Eur. J.* **2017**, *23*, 15543.

[24]　a) P. Marchand, I. A. Hassan, I. P. Parkin, C. J. Carmalt, *Dalt. Trans.* **2013**, *42*, 9406; b) K. L. Choy, *Prog. Mater. Sci.* **2003**, *48*, 57.

[25]　R. M. Cornell, U. Schwertmann, In *Wiley-Vch*; 2003.

[26]　I. Cesar, K. Sivula, A. Kay, R. Zboril, M. Grätzel, *J. Phys. Chem. C* **2009**, *113*, 772.

[27]　Y. Li, L. Zhang, R. Liu, Z. Cao, X. Sun, X. Liu, J. Luo, *ChemCatChem* **2016**, *8*, 2765.

[28]　D. M. Strohmeier, Brian R.; Hercules, *J. Catal.* **1984**, *86*, 266.

[29]　a) M. Chen, X. Wang, Y. H. Yu, Z. L. Pei, X. D. Bai, C. Sun, R. F. Huang, L. S. Wen, *Appl. Surf. Sci.* **2000**, *158*, 134; b) M. N. Islam, T. B. Ghosh, K. L. Chopra, H. N. Acharya, *Thin Solid Films* **1996**, *280*, 20.

[30]　A. Mills, J. Wang, *J. Photochem. Photobiol. A Chem.* **2006**, *182*, 181.

[31]　A. Mills, A. Lepre, N. Elliott, S. Bhopal, I. P. Parkin, S. A. O'Neill, *J. Photochem. Photobiol. A Chem.* **2003**, *160*, 213.

[32]　P. S. Shinde, G. H. Go, W. J. Lee, *J. Mater. Chem.* **2012**, *22*, 10469.

[33]　a) W. Y. Liang, A. D. Yoffe, *Phys. Rev. Lett.* **1968**, *20*, 59; b) T. K. Gupta, *J. Am. Ceram. Soc.* **1990**, *73*, 1817.

[34]　a) A. Kafizas, Y. Ma, E. Pastor, S. R. Pendlebury, C. Mesa, L. Francàs, F. Le Formal, N. Noor, M. Ling, C. Sotelo-Vazquez, C. J. Carmalt, I. P. Parkin, J. R. Durrant, *ACS Catal.* **2017**, *7*, 4896; b) S. Corby, L. Francàs, S. Selim, M. Sachs, C. Blackman, A. Kafizas, J. R. Durrant, *J. Am. Chem. Soc.* **2018**, *140*, 16168; c) F. Le Formal, S. R.

Pendlebury, M. Cornuz, S. D. Tilley, M. Grätzel, J. R. Durrant, *J. Am. Chem. Soc.* **2014**, *136*, 2564; d) Y. Ma, S. R. Pendlebury, A. Reynal, F. Le Formal, J. R. Durrant, *Chem. Sci.* **2014**, *5*, 2964.

[35]   S. R. Pendlebury, X. Wang, F. Le Formal, M. Cornuz, A. Kafizas, S. D. Tilley, M. Grätzel, J. R. Durrant, *J. Am. Chem. Soc.* **2014**, *136*, 9854.

[36]   X. Wang, A. Kafizas, X. Li, S. J. A. Moniz, P. J. T. Reardon, J. Tang, I. P. Parkin, J. R. Durrant, *J. Phys. Chem. C* **2015**, *119*, 10439.

[37]   F. M. Pesci, A. J. Cowan, B. D. Alexander, J. R. Durrant, D. R. Klug, *J. Phys. Chem. Lett.* **2011**, *2*, 1900.

[38]   A. Soudi, P. Dhakal, Y. Gu, *Appl. Phys. Lett.* **2010**, *96*, 253115.

[39]   a) A. C. Larson, R. B. Von Dreele, *Structure* **2004**, *748*, 86; b) B. H. Toby, *J. Appl. Crystallogr.* **2001**, *34*, 210.

[40]   A. Jiamprasertboon, M. J. Powell, S. C. Dixon, R. Quesada-Cabrera, A. M. Alotaibi, Y. Lu, A. Zhuang, S. Sathasivam, T. Siritanon, I. P. Parkin, C. J. Carmalt, *J. Mater. Chem. A* **2018**, *6*, 12682.